

Shape Matching: Evolving Fiber Constraints on a Pneumatic Bilayer

Bilige Yang^{1*}, Joshua Powers^{2*}, Atoosa Parsa², Josh Bongard², and Rebecca Kramer-Bottiglio¹

Abstract—Shape-changing robots that can adapt their physical structure to changing tasks and environments require an ability to locally change their surface curvatures on-demand. Thin shape-shifting sheets represent one approach, and examples using differential growth have shown stimuli-responsive sheets that morph from one shape to another. In this paper, we present pneumatically-actuated bilayer sheets that can morph between shapes using surface fibers that constrain normal expansion while biasing in-plane expansion. The fibers can adhere to the pneumatic sheet to govern its shape trajectory, and can be easily detached and re-attached in various patterns to reconfigure the shape trajectory. We use artificial evolution to solve the geometric inverse problem of determining the fiber placements to attain a target shape upon inflation in simulation. For simple shapes, the evolved solutions converge toward a similar fiber placement strategy. For more complex shapes, evolution finds more diverse fiber patterns, which is desirable since some fiber patterns are more easily fabricated than others. We demonstrate the utility of evolving the fiber patterns in simulation by translating two shapes, a simple saddle and a monkey saddle, from simulation to reality.

I. INTRODUCTION

Incompatible local strains on thin sheets due to in-plane expansion creates out-of-plane buckling; This mechanism explains the morphological change during growth for many processes in botany, such as unfolding of flowers [1] and natural breaking of seed pods [2]. The inverse problem of finding the local differential-growth needed to achieve a desired final shape has been solved analytically in the unconstrained case [3]. Recent demonstrations of shape-shifting sheets have leveraged composite hydrogels [4] and elastomers [5] with localized differential swelling to achieve complex shape changes in response to temperature. However, these systems have relied on suspension in water to counteract gravitational forces, offered slow response times, and are programmed at manufacture to shift to only one target shape. Pneumatically-actuated sheets may be an appealing alternative as they are capable of rapid actuation [6] and high energy density [7]. Pikul *et al.* [8] and Siefert *et al.* [9] presented flat pneumatic structures that can inflate into complex shapes. In these approaches, programmed directionality is permanent and constrained to one fixed motion or shape, and new shapes require the full fabrication of another device.

Here, we introduce a pneumatic bilayer sheet coupled with reconfigurable strain limiting fibers [10], which allows for rapid shape morphing and tunable shape matching. Our

pneumatic bilayer platform achieves uniform in-plane stretch when inflated, with normal expansion limited by evenly distributed thick pillars. Curvatures are attained by attaching strain-limiting fibers to the surface of the bilayer sheet. The strain-limiting fibers we employ here were previously described by Kim, *et al.* [10]. The fibers are coupled to a silicone adhesive such that they can be adhered, removed, and re-adhered in new locations and orientations. When the fibers are applied to the surface of the pneumatic bilayer, local strains are constrained by the fibers, and the strain incompatibility facilitates complex minimal energy shapes [3].

Many pneumatic soft actuators embody constraints with fibers [11] or fabric [12] to limit the strain within a direction and thus determine the inflated shape. For a simple desired motion, such as bending along a single axis, determination of where to place the strain-limiting component is intuitive. Further, the design of pneumatic fiber-reinforced actuators for trajectory matching has been demonstrated for cylindrical actuators [11]. However, in our realization we do not have control over unlimited local stretch and aim to produce complex surface curvatures. Thus, this constrained case falls outside of known analytical solutions.

We attempt the inverse design problem of optimizing strain-limiting fiber placements on a pneumatic bilayer sheet to achieve a desired inflated shape by utilizing an evolutionary algorithm. Artificial evolution has previously been applied to a wide range of inverse design problems such as the design of flapping wing morphologies [13], biological robots [14], and antennae [15]. Our approach employs a canonical genetic algorithm, which searches over the space of all inert fiber patterns, where each pattern is limited to a fixed number of fibers and each fiber has a set of evolved start and end coordinates. Further, we assume that the fibers are straight lines—a simplification that allows us to more easily transfer designs from simulation to reality.

Figure 1 shows our resulting pipeline that takes target curvatures from physical objects or abstract equations as input, optimizes fiber placements that achieve that curvature in simulation, and transfers evolved designs to a real bilayer sheet with low error. When a simple shape is used as input (*e.g.*, a saddle curve), the evolutionary algorithm discovers a fiber pattern similar to the known solution, which verifies that such an approach can find “good” solutions. When a more complex shape is used as input (*e.g.*, a monkey saddle), several distinct but equally efficacious fiber patterns are discovered. In short, we demonstrate that artificial evolution can find surface fiber placements on a 2D expanding sheet given a desired shape.

*These authors contributed equally.

¹Department of Mechanical Engineering Materials Science, Yale University, 10 Hillhouse Avenue, New Haven, CT 06520, USA. (email: rebecca.kramer at yale.edu)

²Department of Computer Science, University of Vermont, 82 University Pl, Burlington, VT 05405, USA.

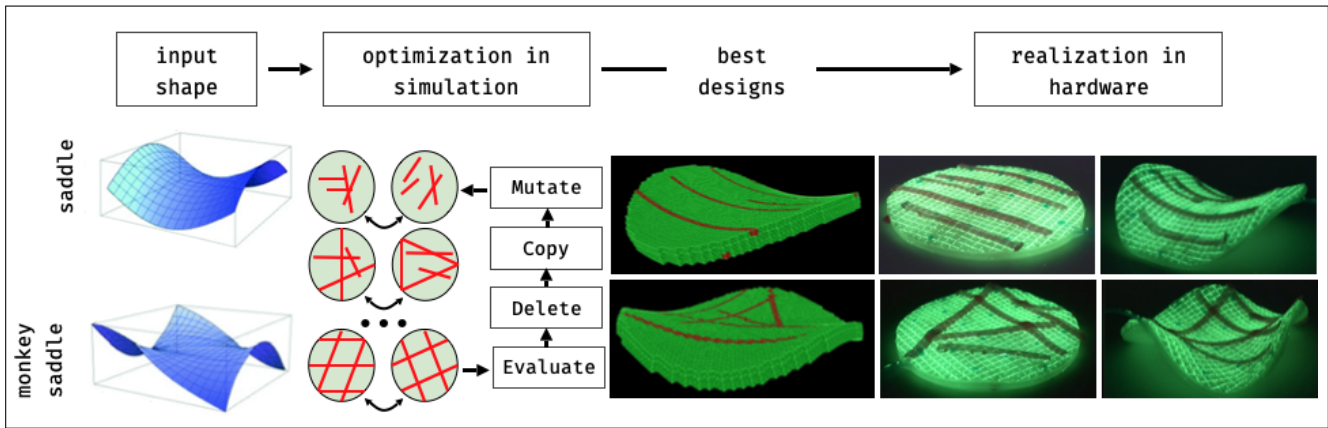


Fig. 1. Beginning with a target shape, we used artificial evolution to discover fiber patterns to match a target shape, then translated the evolved fiber patterns to reality.

II. METHODS

A. Pneumatic Bilayer Sheet

A silicone pneumatic bladder naturally expands in all directions. To constrain expansion in the vertical (z) direction in a pneumatic sheet, we added “pillars” connecting the top and bottom surfaces of the sheet, such that the bladder may only biaxially stretch in the x and y directions.

1) *Fabrication of pneumatic bilayer*: The pneumatic bilayer sheets were made out of molded silicone. Molds were fabricated using laser-cut acrylic parts (Fig. 2a), which were glued together with acrylic adhesive. Two molds were fabricated: one mold for the top silicone membrane with the pillars, and another mold for the bottom silicone membrane. We used EcoFlex 50 elastomer (Smooth-on) with equal parts A and B, and also mixed in luminescent powder for visualization. The mixed silicone was poured into the molds (Fig. 2b). Once cured, we removed the silicone membranes from the molds and adhered them together using pre-cure silicone as a glue (Fig. 2c). A small cut was made on the side of the membrane to insert pneumatic tubing, which was then sealed with silicone adhesive (Silpoxy, Smooth-On).

2) *Fabrication of strain-limiting fiber lamina*: The fabrication of a composite lamina with strain-limiting fibers and adhesive backing was described in prior work [10]. Briefly, polyester threads were embedded into silicone sheets to provide anisotropic strain-limiting behavior. The silicone sheets were coupled to an adhesive silicone (Silbione 4645, Elkem Silicones), which allows patches of the fibers to easily be adhered-to and removed-from surfaces.

3) *Capturing shape with active infrared stereo camera*: To capture the inflated shape of the bilayer, we used an active infrared (IR) stereo camera (D415, Intel Realsense). We painted 20 evenly-distributed dots on the top surface of the bilayer as fiducial markers (Fig. 2d), and captured the coordinates of these points after inflation to compare with simulated coordinates.

B. Simulation

The pneumatic bilayer was simulated with the multi-material physics simulator Voxelyze [16]. In the simulator,

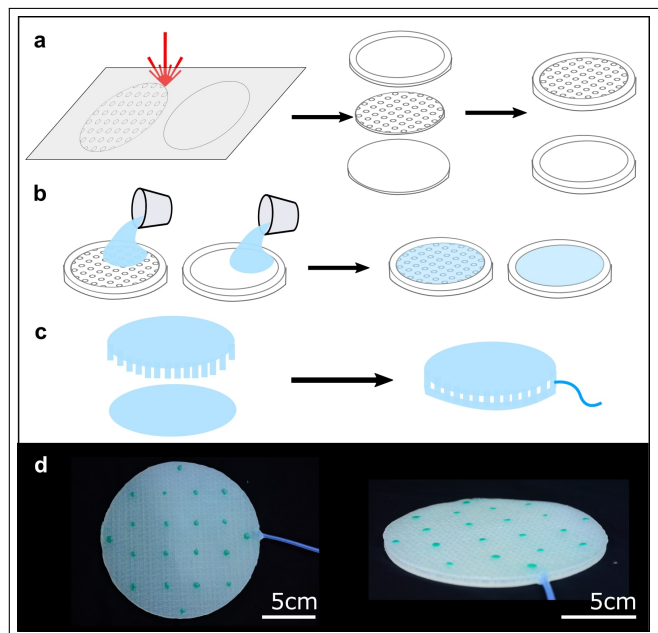


Fig. 2. Fabrication of pneumatic bilayer sheets. **a**: Laser cut acrylic components were glued together with acrylic adhesive. **b**: Silicone was mixed with luminescent powder, poured into acrylic molds, and cured at room temperature. **c**: De-molded silicone layers were adhered using uncured silicone. Pneumatic tubing was inserted and sealed with silicone glue. **d**: Pictures of a pneumatic bladder. Green dots are the twenty fiducial markers. Scale bar = 5cm.

materials are discretized as a collection of cubic elements denoted as voxels. Each voxel is simulated as a point mass connected to its six neighbouring voxels by Euler-Bernoulli beams. To represent the pneumatic bilayer, we created three simulated layers of voxels. The top and the bottom layers were modeled as elastic passive layers ($E = 68900$ Pa), while the middle layer was modeled as an elastic expanding layer ($E = 160000$ Pa) that increased uniformly in volume over the duration of the simulation. Each voxel in the bilayer had a side length of 0.0028 m, with 50 voxels along the diameter of the layer, resulting in a total diameter of 0.14 m (50×0.0028). Lastly, we simulated the strain-limiting fibers by replacing voxels in the top and bottom layers

with stiff/inelastic voxels ($E = 9000000$ Pa). Our simulation neglected contact with the ground and gravity. We note that we calibrated the simulator to these physical parameters by hand until we observed visual matching between simulation and reality.

C. Experimental Design

To assess the fidelity of our inverse design approach, we conducted experiments on two representative desired shapes. The first is the well-known and well-understood saddle shape (Fig. 1) with negative Gaussian curvature [17]. The second shape, the “monkey saddle” (Fig. 1), was chosen for its slightly more complex mathematical formulation [18].

1) *Simple case—saddle*: For the simple saddle, we started with the known solution of limiting strain in orthogonal directions on the top and bottom of the sheet (*i.e.*, limiting x -direction stretch on the top surface and limiting y -direction stretch on the bottom surface). We tested this design in reality and achieved the desired saddle shape. We then translated the fiber placements to simulation to validate that the simulated sheet produced the same inflated shape as the physical sheet (the forward problem). Finally, we used the generated shape in simulation as the target shape for the evolutionary algorithm to match using evolved sets of fiber placements (the inverse problem).

2) *Complex case—monkey saddle*: For the monkey saddle shape, we used the known mathematical function, $f(x, y) = x^3 - 3xy^2$, to generate the input target shape, then used the evolutionary algorithm to discover fiber placements that should generate the target shape in the inflated pneumatic bilayer (the inverse problem only).

3) *Sim2Real validation and error categorization*: We used two error metrics in our study: simulation error and transfer error. Simulation error represents the error between a target shape and a computer generated design, during the optimization process with the evolutionary algorithm. Transfer error represents the error between the physical realization and computer generated design (calculated as the percentage error between heights of the 20 fiducial markers in reality and in simulation). Simulation error measures the ability of the algorithm to match a target shape, while transfer error validates that the computer generated design can be replicated in reality.

As described in §II.B., we employed a soft-body finite-element simulation in which the elements take the form of small cubical volumes: voxels. We used the height of the voxels on the sheet to compare different shapes. The uninflated sheet provided the baseline heights of all voxels, and the inflated sheet deviated from the baseline by some height difference. Our optimization function aimed to minimize the error between the target and evolved voxel heights, given as:

$$e_s = \frac{\sum_{i=0}^n |s_i - t_i|}{\sum_{i=0}^n |t_i - u_i|} \quad (1)$$

where e_s is the error in simulation, n is the number of voxels, s_i is the height of voxel i on the evolved (simulated) shape,

t_i is the height of voxel i on the target shape, and u_i is the height of voxel i on the uninflated baseline.

The transfer error is computed similarly but rather based on the 20 fiducial markers mentioned. Each marker corresponds to 4 voxels on the simulated designs. Thus, the transfer error can be computed as:

$$e_t = \frac{\sum_{j=0}^m |s_j - r_j|}{\sum_{j=0}^m |r_j - u_j|} \quad (2)$$

where e_t is the reality transfer error, m is the number of markers, s_j is the average height of the four marked voxels on the evolved (simulated) shape corresponding to marker j in reality, r_j is the height of marker j on the real bilayer, and u_j is the average height of the four marked voxels on the uninflated baseline that correspond to marker j in reality.

D. The Evolutionary Algorithm

Evolutionary algorithms are a class of population-based, gradient-free optimization methods [19]. In most such algorithms, at each generation, individuals in a population are evaluated based on some fitness measure and individuals with better fitness values are selected to reproduce in the next generation.

We used a canonical genetic algorithm [20] to evolve fiber patterns on the expanding sheet. We used a direct encoding scheme for the genome, where the genotype indicates the starting and ending points of the fibers on the bottom and top surfaces of the sheet. The genetic algorithm was implemented with elitism, with an elite size of one: the individual with the highest fitness in each generation survives to the next, without any changes to its genome. The fitness function was to reduce error as described in Eq. 1.

To produce the next generation, we did not implement crossover but instead utilized a two-way tournament selection (with replacement), followed by a mutation on the selected individual. The mutation randomly selects one of the fiber endpoints and changes its position on the surface by drawing a new (x, y) end position from a uniform distribution the size of the total sheet. In other words, the new endpoint position can be anywhere on the sheet’s surface. To fill in the fiber locations between the starting and ending points on the simulated sheet we employed Bresenham’s digital line plotting algorithm [21].

For each of the two target shapes, we ran the evolutionary algorithm with a population size $p = 20$, for $g = 120$ generations (*i.e.*, 120 generations is one independent trial). Population size and number of generations were restricted to these low numbers, since the bladder was simulated in a CPU-based soft body simulator (described in section §II.B.) and evaluating each individual takes considerable time (≈ 22 seconds on a Quad-Core Intel Core i7 Macbook Pro). Despite this low search effort, significant decreases in error were achieved, as demonstrated in the next section.

We conducted three independent trials each for the normal saddle and for the monkey saddle. Only a small number of trials was possible, as each trial ran on average a little over 14 hours. Lastly, we limited the number of fibers generated to

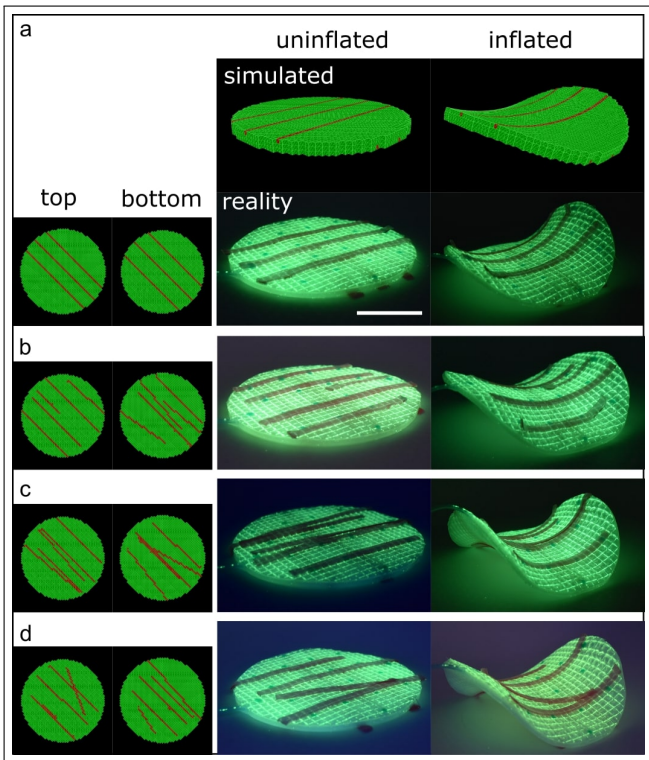


Fig. 3. Inflated saddle shapes with different strain-limiting fiber placements. Left column shows top-down and bottom-up views of fiber placements on the top and bottom of the sheet in simulation. Illuminated sheets are physical hardware instantiations. **a**: Hand-designed fiber placement. Three fibers on top and three fibers on bottom making perpendicular angles. Scale bar = 5 cm. **b-e**: Evolved fiber placements (designs 1-3). All placements were able to generate the simple saddle shape with a moderate transfer error ($\approx 10\%$).

be five fibers per face (top and bottom) for the simple saddle case to simplify future transfer to reality. We increased this limit to seven fibers per face for the monkey saddle case, due to its more complicated final curvatures.

III. RESULTS

A. Simple saddle

The best evolved designs from the three independent trials for the saddle, shown in Fig. 3b-d, embodied a set of fiber placements similar to the hand-designed set of fiber placements (the known solution, shown in Fig. 3a). This result indicates that the evolutionary algorithm “rediscovered” known optimal designs. On average, the evolved designs achieved a small simulation error—the error between the target shape and evolved shape in simulation—of $\approx 3.12\%$, with the lowest simulation error of 2.79% (see Table I). On average, the physical realization achieved a moderate transfer error—the error between the physical bladder and simulated (evolved) bladder—of $\approx 11.45\%$, with the lowest transfer error of 10.31%. We note that the simulation errors are similar across designs, as are transfer errors, demonstrating the reliability and reproducibility of our pipeline.

B. Monkey saddle

To test our pipeline on a more complex shape with no known solutions, we chose the monkey saddle shape—a

TABLE I
RESULTS SUMMARY FOR THE SADDLE CURVATURE.

Design	Simulation Error	Transfer Error
1	3.37%	10.31%
2	2.79%	11.11%
3	3.19%	12.93%

saddle with three valleys and three mountains—as shown in Figure 4. The shape was generated with the equation: $f(x, y) = x^3 - 3xy^2$. The output of this equation was then normalized within the range $[a, b]$, where a was the minimum voxel height attained from the simple saddle and b the maximum voxel height. Using this target shape input, the algorithm was able to achieve solutions with an average simulation error of $\approx 11.13\%$, with the lowest at 10.16%, and an average transfer error of $\approx 15.84\%$, with the lowest at 14.67%. It is worth noting that both the simulation and transfer errors for the monkey saddle are higher than the errors for the simple saddle, possibly due to the increased complexity of the target monkey saddle shape.

TABLE II
RESULTS SUMMARY FOR THE MONKEY SADDLE CURVATURE.

Design	Simulation Error	Transfer Error
1	11.57%	16.67%
2	11.66%	14.67%
3	10.16%	16.19%

C. Error minimization and solution diversity

We show the simulation error during evolution for both the saddle and monkey saddle designs in Figure 5. The simulation error for the saddle continues to drop until the end of the 120 generations, while the simulation error for the monkey saddle decreases faster at first but plateaus after the 60th cycle. This discrepancy could potentially be mitigated by employing an evolutionary algorithm based on Age-Fitness Pareto Optimization (AFPO) [22], a multi-objective optimization method for avoiding premature convergence.

We note here that while the generated curvatures from each evolved solution in Figures 3 and 4 appear globally similar, the fiber placements converge more in the simple saddle case. For the simple saddle, the fiber placements from each trial (design) are visually similar, and this convergence suggests the existence of one underlying solution for the saddle shape. For the monkey saddle, the evolved fiber placements are more visually different, which could mean that increasing shape complexity corresponds to a wider variety of possible fiber pattern solutions.

To measure the degree of convergence for the evolved solutions quantitatively, we compared the different designs using the Hausdorff distance metric, which has previously been used to compare the similarity of images [23]. We have adapted this distance metric for use here by representing an evolved fiber design on the upper or lower surface as a binary 50×50 matrix in which unity values represent areas

of the surface covered by fibers and nullity values represent uncovered areas. The distance metric can then be written as

$$H(A, B) = \max(h(A, B), h(B, A)) \quad (3)$$

where A and B are the sets of points/pixels in two evolved designs A and B , in either the upper or lower surface, and $h(A, B) = \max_{a \in A} \min_{b \in B} \|a - b\|$. Here, a and b are non-zero points in A and B . The function $h(A, B)$ identifies the point $a \in A$ that is farthest from any point of $b \in B$ and measures the distance from a to its nearest neighbour in B [23]. $H(A, B)$ then indicates how far one pattern has to “expand” in order to “cover” the other pattern. $H(A, B) = 0$ means the two patterns are identical. The larger $H(A, B)$ is, the more different the two patterns are.

TABLE III

HAUSDORFF DISTANCES BETWEEN EVOLVED FIBER PATTERN DESIGNS.

Simple saddle (Top surface)	Design 1	Design 2	Design 3
Design 1	0	8.0	8.0
Design 2	-	0	6.1
Design 3	-	-	0
Simple Saddle (Bottom surface)	Design 1	Design 2	Design 3
Design 1	0	12.1	7.6
Design 2	-	0	7.6
Design 3	-	-	0
Monkey Saddle (Top surface)	Design 1	Design 2	Design 3
Design 1	0	10.2	10.3
Design 2	-	0	7.0
Design 3	-	-	0
Monkey Saddle (Bottom surface)	Design 1	Design 2	Design 3
Design 1	0	14.3	10.8
Design 2	-	0	25.1
Design 3	-	-	0

We computed the Hausdorff metric H between the fiber patterns evolved to match the simple saddle and the monkey saddle shapes, for both the top and bottom sheet surfaces (Table III). The average distance between the designs evolved to match the simple saddle (8.23; average of top two panels in Table III) is lower than the average distance between designs evolved to match the monkey saddle (12.95; average of bottom two panels in Table III). This result confirms the qualitative observation that evolved fiber designs for the simple saddle are more similar to each other while the evolved fiber designs for the monkey saddle are more diverse. We conducted two control trials in which 36 random fiber patterns were generated—one with five fibers on both the top and bottom surfaces, and another with seven fibers on each surface—and computed the Hausdorff distances between each pattern according to Equation 3. The average of these metrics was 17.98 for the random five-fiber patterns and 16.33 for the random seven-fiber patterns. These two numbers are larger than the average of all of our metrics in the table above, which was 11.08, indicating that our algorithm does find sets of solutions that are more similar than random solution sets.

IV. CONCLUSION AND FUTURE WORK

In this paper, we introduced a pneumatic bilayer sheet with reconfigurable strain-limiting surface fibers that enable

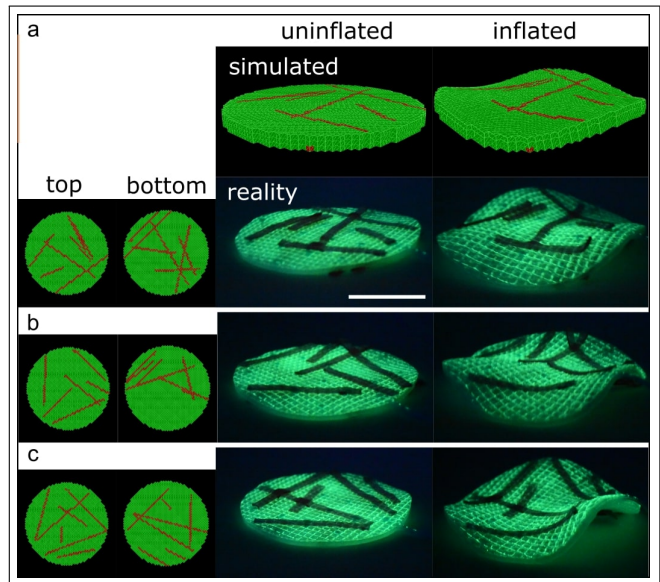


Fig. 4. Inflated monkey saddle shapes with different evolved strain-limiting fiber placements. Left column shows top-down and bottom-up views of fiber placements on the top and bottom of the sheet in simulation. Illuminated sheets on the right are physical hardware instantiations. **a-c**: Evolved fiber placements (designs 1-3). All placements were able to generate a monkey saddle-like shape. Scale bar = 5 cm.

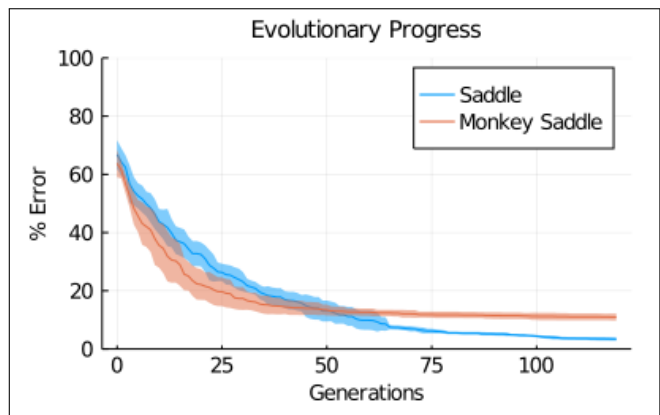


Fig. 5. Simulation Error between evolved shape and target shape, over 120 generations for the simple saddle and the monkey saddle shapes. The solid curves represent the average error for all designs; Shaded regions show one standard deviation of the averaged error.

the sheet to morph into different shapes upon inflation. We have also demonstrated a sample pipeline for automatically designing the placement of the strain-limiting fibers on the pneumatic sheet to induce a desired curvature. We have shown that evolutionary search is a promising approach that repeatedly converged on a known solution for a simple target shape (saddle curvature), and produced a diversity of convincing results for a more complex target shape (monkey saddle curvature). We believe this pipeline could extend to the design of fiber patterns that produce increasingly complex shapes in pneumatic sheets via improvements in the bilayer construction, the use of more fibers, and/or stronger search methods that may enable the discovery of additional patterns.

Although formal methods for deriving strain limitation

are possible for complex shapes, such methods assume perfect control over local strain at all points and tend to be mathematically burdensome. Thus, empirical approaches like evolutionary algorithms can be reasonable alternatives. Evolutionary algorithms are particularly well-suited to optimizations in which the number of parameters is not fixed [24], [25]. For the design space herein, additional objectives could include rewarding less total fiber material, fewer numbers of fibers, fewer fiber crossing points, or making fibers with non-zero curvatures. Such multi-objective optimization could be employed as a method to reduce either the simulation error (indicating “better” solutions) or transfer error (indicating more manufacturable solutions).

Finally, our implementation of reconfigurable fibers on a pneumatic bilayer sheet allowed us to use the same pneumatic bilayer for all experiments herein. With continued progress toward variable tensile stiffness materials [26], [27], our pipeline could be used to develop shape-changing sheets that can autonomously adapt without any human handling. Evolving fiber placements could also augment existing evolutionary algorithms that already simultaneously optimize the shapes, material properties, and control policies of soft robots [28], [29], [30], thus paving the way toward automated shape-changing robots that adapt to different environments and tasks [31].

ACKNOWLEDGMENT

This material is based upon work supported by the National Science Foundation under the Emerging Frontiers in Research and Innovation (EFRI) program (EFMA-1830870).

REFERENCES

- [1] E. Reyssat and L. Mahadevan, “Hygromorphs: from pine cones to biomimetic bilayers,” *Journal of the Royal Society Interface*, vol. 6, no. 39, pp. 951–957, 2009.
- [2] S. Armon, E. Efrati, R. Kupferman, and E. Sharon, “Geometry and mechanics in the opening of chiral seed pods,” *Science*, vol. 333, no. 6050, pp. 1726–1730, 2011.
- [3] W. M. van Rees, E. Vouga, and L. Mahadevan, “Growth patterns for shape-shifting elastic bilayers,” *Proceedings of the National Academy of Sciences*, vol. 114, no. 44, pp. 11 597–11 602, 2017.
- [4] A. S. Gladman, E. A. Matsumoto, R. G. Nuzzo, L. Mahadevan, and J. A. Lewis, “Biomimetic 4d printing,” *Nature materials*, vol. 15, no. 4, pp. 413–418, 2016.
- [5] J. W. Boley, W. M. van Rees, C. Lissandrello, M. N. Horenstein, R. L. Truby, A. Kotikian, J. A. Lewis, and L. Mahadevan, “Shape-shifting structured lattices via multimaterial 4d printing,” *Proceedings of the National Academy of Sciences*, vol. 116, no. 42, pp. 20 856–20 862, 2019.
- [6] B. Mosadegh, P. Polygerinos, C. Keplinger, S. Wennstedt, R. F. Shepherd, U. Gupta, J. Shim, K. Bertoldi, C. J. Walsh, and G. M. Whitesides, “Pneumatic networks for soft robotics that actuate rapidly,” *Advanced functional materials*, vol. 24, no. 15, pp. 2163–2170, 2014.
- [7] M. Wehner, M. T. Tolley, Y. Mengüç, Y.-L. Park, A. Mozeika, Y. Ding, C. Onal, R. F. Shepherd, G. M. Whitesides, and R. J. Wood, “Pneumatic energy sources for autonomous and wearable soft robotics,” *Soft robotics*, vol. 1, no. 4, pp. 263–274, 2014.
- [8] J. Pikul, S. Li, H. Bai, R. Hanlon, I. Cohen, and R. Shepherd, “Stretchable surfaces with programmable 3d texture morphing for synthetic camouflaging skins,” *Science*, vol. 358, no. 6360, pp. 210–214, 2017.
- [9] E. Siéfert, E. Reyssat, J. Bico, and B. Roman, “Bio-inspired pneumatic shape-morphing elastomers,” *Nature materials*, vol. 18, no. 1, pp. 24–28, 2019.
- [10] S. Y. Kim, R. Baines, J. Booth, N. Vasios, K. Bertoldi, and R. Kramer-Bottiglio, “Reconfigurable soft body trajectories using unidirectionally stretchable composite laminae,” *Nature communications*, vol. 10, no. 1, pp. 1–8, 2019.
- [11] F. Connolly, C. J. Walsh, and K. Bertoldi, “Automatic design of fiber-reinforced soft actuators for trajectory matching,” *Proceedings of the National Academy of Sciences*, vol. 114, no. 1, pp. 51–56, 2017.
- [12] Y. Sun, Y. S. Song, and J. Paik, “Characterization of silicone rubber based soft pneumatic actuators,” in *2013 IEEE/RSJ International Conference on Intelligent Robots and Systems*. Ieee, 2013, pp. 4446–4453.
- [13] K. Rosser, J. Kok, J. Chahl, and J. Bongard, “Sim2real gap is non-monotonic with robot complexity for morphology-in-the-loop flapping wing design,” in *2020 IEEE International Conference on Robotics and Automation (ICRA)*, 2020, pp. 7001–7007.
- [14] S. Kriegman, D. Blackiston, M. Levin, and J. Bongard, “A scalable pipeline for designing reconfigurable organisms,” *Proceedings of the National Academy of Sciences*, vol. 117, no. 4, pp. 1853–1859, 2020. [Online]. Available: <https://www.pnas.org/content/117/4/1853>
- [15] J. D. Lohn, G. S. Hornby, and D. S. Linden, “Human-competitive evolved antennas,” *Artificial Intelligence for Engineering Design, Analysis and Manufacturing: AI EDAM*, vol. 22, no. 3, p. 235, 2008.
- [16] J. Hiller and H. Lipson, “Dynamic simulation of soft multimaterial 3d-printed objects,” *Soft robotics*, vol. 1, no. 1, pp. 88–101, 2014.
- [17] B. O’neil, *Elementary differential geometry*. Academic press, 2014.
- [18] S. D. Peckham, “Monkey, starfish and octopus saddles,” *Proceedings of Geomorphometry*, pp. 31–34, 2011.
- [19] X. Yu and M. Gen, *Introduction to evolutionary algorithms*. Springer Science & Business Media, 2010.
- [20] D. E. Goldberg, *Genetic Algorithms in Search, Optimization and Machine Learning*, 1st ed. USA: Addison-Wesley Longman Publishing Co., Inc., 1989.
- [21] J. E. Bresenham, “Algorithm for computer control of a digital plotter,” *IBM Systems journal*, vol. 4, no. 1, pp. 25–30, 1965.
- [22] M. Schmidt and H. Lipson, “Age-fitness pareto optimization,” in *Genetic programming theory and practice VIII*. Springer, 2011, pp. 129–146.
- [23] D. P. Huttenlocher, G. A. Klanderman, and W. J. Rucklidge, “Comparing images using the hausdorff distance,” *IEEE Transactions on pattern analysis and machine intelligence*, vol. 15, no. 9, pp. 850–863, 1993.
- [24] Z. Chen and B. Li, “Efficient evolution for neural architecture search,” in *2020 International Joint Conference on Neural Networks (IJCNN)*, 2020, pp. 1–7.
- [25] K. O. Stanley, D. B. D’Ambrosio, and J. Gauci, “A hypercube-based encoding for evolving large-scale neural networks,” *Artificial Life*, vol. 15, no. 2, pp. 185–212, 2009.
- [26] T. L. Buckner, M. C. Yuen, S. Y. Kim, and R. Kramer-Bottiglio, “Enhanced variable and variable stiffness and stretchability enabled by phase-changing particulate additives,” *Advanced Functional Materials*, vol. 29, no. 50, p. 1903368, 2019.
- [27] J. Santoso, E. H. Skorina, M. Salerno, S. de Rivaz, J. Paik, and C. D. Onal, “Single chamber multiple degree-of-freedom soft pneumatic actuator enabled by adjustable stiffness layers,” *Smart Materials and Structures*, vol. 28, no. 3, p. 035012, 2019.
- [28] D. S. Shah, J. P. Powers, L. G. Tilton, S. Kriegman, J. Bongard, and R. Kramer-Bottiglio, “A soft robot that adapts to environments through shape change,” *Nature Machine Intelligence*, vol. 3, no. 1, pp. 51–59, 2021.
- [29] S. Kriegman, A. M. Nasab, D. Shah, H. Steele, G. Branin, M. Levin, J. Bongard, and R. Kramer-Bottiglio, “Scalable sim-to-real transfer of soft robot designs,” in *2020 3rd IEEE International Conference on Soft Robotics (RoboSoft)*. IEEE, 2020, pp. 359–366.
- [30] J. Powers, R. Grindle, S. Kriegman, L. Frati, N. Cheney, and J. Bongard, “Morphology dictates learnability in neural controllers,” in *Artificial Life Conference Proceedings*. MIT Press, 2020, pp. 52–59.
- [31] D. Shah, B. Yang, S. Kriegman, M. Levin, J. Bongard, and R. Kramer-Bottiglio, “Shape changing robots: Bioinspiration, simulation, and physical realization,” *Advanced Materials*, p. 2002882, 2020.